

# Microscopic quasifission dynamics of the $^{54}\text{Cr} + ^{243}\text{Am}$ reaction

Liang Li (李良)<sup>1</sup> and Lu Guo (郭璐)<sup>1,\*</sup>

<sup>1</sup>*School of Nuclear Science and Technology, University of Chinese Academy of Sciences, Beijing 100049, China*

(Dated: March 10, 2026)

**Background:** The synthesis of superheavy elements (SHEs) beyond Oganesson, such as  $Z = 119$ , remains a formidable challenge, primarily because the dominant quasifission (QF) channel severely hinders the formation of compound nuclei. A microscopic understanding of the QF dynamics is therefore essential for guiding future experiments.

**Purpose:** We investigate the microscopic mechanisms of QF in the  $^{54}\text{Cr} + ^{243}\text{Am}$  reaction, a key candidate system for synthesizing SHE 119, with particular emphasis on the roles of projectile orientation and incident energy.

**Method:** The calculations are performed using the fully microscopic time-dependent Hartree-Fock theory based on the Skyrme energy density functional. We perform systematic simulations covering a broad set of initial orientations of the deformed  $^{54}\text{Cr}$  and  $^{243}\text{Am}$  nuclei, together with a finely spaced range of incident energies extending from below to well above the Coulomb barrier.

**Results:** Our simulations at fixed energy show that projectile side collisions are governed by shell effects driving heavy and light fragments toward spherical  $Z = 82$  and deformed  $N = 52$ – $56$  closures, respectively, whereas tip collisions exhibit weaker shell influence. These shell-dominated reactions are characterized by shorter interaction times, attributed to the enhanced rigidity of shell-stabilized fragments accelerating neck rupture. Furthermore, the energy dependence reveals a complex evolution where the system transitions from an octupole-stabilized regime ( $Z \approx 88$ ) to a spherical shell-driven regime, with specific energy windows exhibiting suppressed shell influence.

**Conclusions:** Our microscopic study demonstrates that the manifestation of shell effects in the final QF fragment distributions is a dynamical outcome sensitively dependent on both the initial collision geometry and the incident energy. This pronounced energy dependence suggests that the competition between QF and fusion can be tuned. Systematically probing this energy sensitivity is crucial for identifying optimal incident energies where the QF process exhibits suppressed shell influence, thereby potentially enhancing the fusion probability and improving the prospects for synthesizing new SHEs.

## I. INTRODUCTION

The synthesis of superheavy elements (SHEs) has long been a central pursuit in nuclear physics, motivated by the quest to determine the upper limit of atomic number and to verify the existence of the “island of stability” governed by quantum shell effects [1,2]. To date, SHEs up to  $Z = 118$  have been successfully synthesized through heavy-ion fusion reactions, using either “cold fusion” with  $^{208}\text{Pb}$  or  $^{209}\text{Bi}$  targets or “hot fusion” with a  $^{48}\text{Ca}$  beam on actinide targets [3–6]. Despite these achievements, all major attempts over the past decade to extend the periodic table into the eighth period by synthesizing elements 119 and 120 have been unsuccessful [7–10]. This challenge primarily stems from the fact that  $^{48}\text{Ca}$ -induced reactions are no longer feasible due to the limited availability of target isotopes such as einsteinium and fermium. As a result, heavier projectiles, such as  $^{50}\text{Ti}$ ,  $^{51}\text{V}$ , and  $^{54}\text{Cr}$ , are now being employed in reactions with actinide targets. Recently, the Lawrence Berkeley National Laboratory (LBNL) in the United States successfully synthesized  $^{290}\text{Lv}$  via the  $^{50}\text{Ti} + ^{244}\text{Pu}$  reaction, demonstrating the feasibility of using projectiles heavier than  $^{48}\text{Ca}$  for SHE synthesis [11]. This breakthrough has renewed

confidence in the pursuit of elements 119 and 120 using similar reactions. Meanwhile, the Institute of Modern Physics (IMP), Chinese Academy of Sciences is preparing to explore element 119 through the  $^{54}\text{Cr} + ^{243}\text{Am}$  system at the upgraded HIRFL-CAFE2 facility [12].

While these experimental breakthroughs have sparked renewed optimism, synthesizing elements 119 and 120 remains an exceptionally challenging task. The primary obstacle stems from the combined prohibitive effects of quasifission (QF) and fusion-fission. QF dominates the dynamical evolution from the captured dinuclear system toward a fully equilibrated compound nucleus. This causes the system to re-separate before achieving full equilibration, thereby significantly suppressing the formation probability [13–15]. Even if a compound nucleus is formed, its low fission barrier makes it highly susceptible to fission. As a result, evaporation-residue cross sections are suppressed to the femtobarn level (or even lower) for the synthesis of elements 119 and 120. Providing reliable theoretical predictions for these reactions presents a formidable challenge, as QF dynamics arise from a subtle interplay between entrance- and exit-channel degrees of freedom, including the collision energy [16–18], the deformation and orientation of the colliding nuclei [19–21], the neutron-to-proton asymmetry of the composite system [22–25], and the shell effects in the emerging fragments [26–28]. These factors, individu-

\* [lguo@ucas.ac.cn](mailto:lguo@ucas.ac.cn)

ally or collectively, govern the trajectory of the dinuclear system and determine whether it evolves toward fusion or re-separates.

To capture these intricate dynamics, the theoretical description of QF spans a wide spectrum of models. On the macroscopic side, approaches such as the dinuclear system model [29–33], stochastic Langevin-type equations [34], and the dynamical cluster-decay model [35] have been successfully developed. In these phenomenological frameworks, the complex many-body problem is effectively reduced to the evolution of a few key collective degrees of freedom, such as the internuclear distance and mass asymmetry, driven by conservative potentials and dissipative forces. On the microscopic front, semi-classical transport theories, including the Quantum Molecular Dynamics [36–38] and Boltzmann-Uehling-Uhlenbeck models [39], are widely employed to simulate the evolution based on the motion of nucleons and explicit nucleon-nucleon collision terms. By tracking the phase-space evolution and incorporating two-body scattering, these transport approaches provide robust descriptions of fragmentation and fluctuation phenomena. Furthermore, advanced frameworks, including stochastic mean-field theory [40,41] and the time-dependent random phase approximation [42,43] which extend beyond the standard mean-field approximation, as well as relativistic covariant density functional theory [44], have also been applied to QF studies.

Among these approaches, the time-dependent Hartree-Fock (TDHF) theory stands out as the most foundational microscopic framework for low-energy heavy-ion dynamics [45–50]. In contrast to the macroscopic and semi-classical models discussed above, TDHF provides a fully microscopic, self-consistent description without the need for empirical parameters specific to the reaction mechanism [51–55]. By dynamically evolving the self-consistent mean field, the theory naturally incorporates essential physical effects such as nuclear deformation and orientation dependence [56–60], nucleon transfer [61–65], and one-body dissipation [66–68]. Consequently, TDHF has achieved remarkable success in reproducing experimental observables across a wide range of phenomena, including fusion [69–74], fission [75–79], multinucleon transfer [80–82], resonance dynamics [83–85] and, crucially, QF reactions [23,86,87]. Recent TDHF studies have demonstrated close agreement with data on mass-angle correlations and fragment mass distributions [88–90], while offering deep insights into the steering role of spherical and deformed shell closures [91–93]. These successes firmly establish TDHF as a powerful predictive tool to investigate the microscopic mechanisms governing the QF process.

Motivated by these successes, in this work, we apply the TDHF method to the  $^{54}\text{Cr} + ^{243}\text{Am}$  system, a prime candidate for synthesizing element 119. Our objective is to provide a comprehensive microscopic investigation of the QF mechanisms in this reaction, with a specific focus on the combined influence of the incident energy and

the initial orientations of the deformed reactants. The remainder of this article is organized as follows: Section II outlines the theoretical framework and computational details. The simulation results and detailed discussions are presented in Section III. Finally, a summary of our findings is provided in Section IV.

## II. THEORETICAL FRAMEWORK

The fundamental assumption of the TDHF theory is that the nuclear many-body wave function  $\Psi(t)$  remains a single Slater determinant at all times,

$$\Psi(t) = \mathcal{A}(\phi_1(\mathbf{r}_1, t)\phi_2(\mathbf{r}_2, t)\dots\phi_A(\mathbf{r}_A, t)), \quad (1)$$

where  $\mathcal{A}$  is the antisymmetrization operator and  $\phi_i(\mathbf{r}, t)$  are the  $A$  occupied single-particle wave functions. The time evolution of these wave functions is governed by the TDHF equations,

$$i\hbar \frac{\partial}{\partial t} \phi_i(\mathbf{r}, t) = \hat{h}(t)\phi_i(\mathbf{r}, t), \quad (2)$$

which can be derived from the time-dependent variational principle. The self-consistent single-particle hamiltonian  $\hat{h}(t)$  is constructed from the Skyrme energy density functional. In this work, we employ the SLy5 Skyrme parametrization [94]. It is crucial to note that the standard Sky3D code [95] does not include the contributions from the squared spin-current tensor density (the so-called  $J^2$  terms) that were included in the SLy5 fit. As a result, a fully consistent realization of the SLy5 energy density functional requires an explicit implementation of these  $J^2$  terms. To ensure such consistency, we utilize a modified version of Sky3D in which the  $J^2$  terms are explicitly incorporated, as has been successfully applied in previous works [28,71,72,78,82,92,96–99]. The set of coupled nonlinear TDHF equations is solved on a three-dimensional Cartesian coordinate system without any symmetry restrictions.

Within this coordinate representation, the initial state for the time evolution is constructed from the ground-state wave functions of the projectile and target nuclei, which are obtained via the static Hartree-Fock (HF) method with the same SLy5 functional. Nuclear multipole deformations are naturally incorporated into the ground states. Table I summarizes the calculated deformation parameters based on this full functional. These static properties define the initial geometric configurations for the subsequent dynamical simulations. For the projectile  $^{54}\text{Cr}$ , the calculation yields a pronounced prolate shape characterized by  $\beta_{20} \approx 0.218$  with vanishing triaxiality. This axial symmetry implies that the orientation effects can be effectively captured by considering the two limiting configurations. Therefore, we define two distinct orientations for  $^{54}\text{Cr}$ : the tip orientation with  $\theta_P = 0^\circ$ , where the projectile's symmetry axis is parallel to the beam, and the side orientation with

TABLE I. Ground-state deformation parameters for the projectile  $^{54}\text{Cr}$  and the target  $^{243}\text{Am}$ , calculated using the Hartree-Fock method with the Skyrme SLy5 parametrization.

Nucleus	$\beta_{20}$	$\beta_{22}$	$\beta_{30}$	$\beta_{40}$	$\beta_{50}$	$\beta_{60}$
$^{54}\text{Cr}$	0.218	0.000	0.000	0.063	0.000	-0.004
$^{243}\text{Am}$	0.282	0.000	-0.053	0.132	-0.023	0.022

$\theta_P = 90^\circ$ , where the symmetry axis is perpendicular to the beam. Regarding the target  $^{243}\text{Am}$ , the ground state exhibits a complex deformation pattern. As listed in Table I, it possesses a large quadrupole deformation of  $\beta_{20} \approx 0.282$ , augmented by a significant hexadecapole component of  $\beta_{40} \approx 0.132$ . Crucially, the non-vanishing odd-multipole deformations,  $\beta_{30}$  and  $\beta_{50}$ , explicitly break the reflection symmetry and result in a characteristic pear-like shape. Consequently, the configuration with  $\theta_T = 0^\circ$ , corresponding to the blunt end, is physically distinct from that with  $\theta_T = 180^\circ$ , corresponding to the narrow end. To account for this asymmetry, we must sample the target orientation  $\theta_T$  over the full range of  $0^\circ \leq \theta_T \leq 180^\circ$ . Accordingly, nine initial target orientations are selected:  $0^\circ, 30^\circ, 45^\circ, 60^\circ, 90^\circ, 120^\circ, 135^\circ, 150^\circ$ , and  $180^\circ$ .

For the dynamical evolutions, we use a numerical box of  $60 \times 28 \times 48 \text{ fm}^3$ , with a grid spacing of 1.0 fm and a time step of 0.2 fm/c. The initial separation distance between the centers of mass of the projectile and the target is set to 26 fm. A boost is then applied to accelerate the nuclei along a Coulomb trajectory to a specified center-of-mass energy  $E_{c.m.}$ . For each orientation combination  $(\theta_P, \theta_T)$ , we perform a systematic scan of the impact parameter  $b$ , starting from  $b = 0 \text{ fm}$  with an increment of  $\Delta b = 0.5 \text{ fm}$ , until the reaction becomes quasielastic. The time evolution is halted when the relative distance between the final fragments exceeds 26 fm, at which point the final scattering angle is determined by Coulomb trajectory propagation.

The angle-averaged yield  $\sigma_\lambda$  for a specific reaction channel  $\lambda$  is quantified by integrating over the impact parameter and averaging over all initial orientations,

$$\sigma_\lambda \propto \int_{b_{\min}}^{b_{\max}} b db \int_0^{\frac{\pi}{2}} d\theta_P \sin(\theta_P) \int_0^\pi d\theta_T \sin(\theta_T) P_b^\lambda(\theta_P, \theta_T), \quad (3)$$

where  $P_b^\lambda(\theta_P, \theta_T)$  is the probability (either 0 or 1 for a single TDHF run) that the event at a given impact parameter  $b$  and orientation configuration  $(\theta_P, \theta_T)$  results in channel  $\lambda$ .

### III. RESULTS AND DISCUSSION

To interpret the subsequent dynamical simulations, we first analyze the entrance channel properties via the nucleus-nucleus interaction potentials  $V(R)$ . Figure 1 presents these potentials for the  $^{54}\text{Cr} + ^{243}\text{Am}$  system,

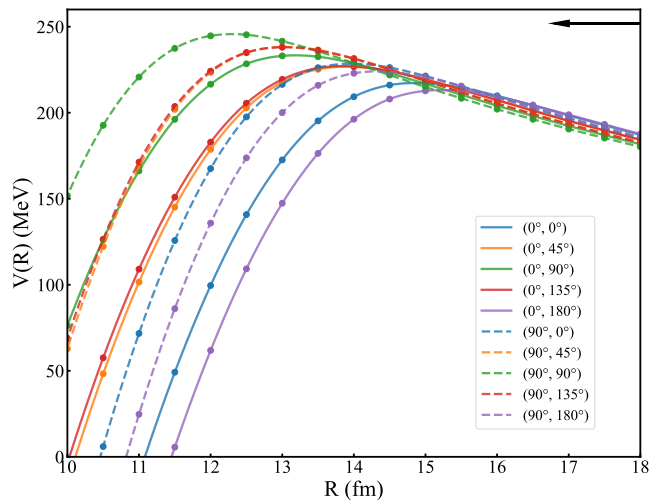


FIG. 1. Internuclear potentials for the  $^{54}\text{Cr} + ^{243}\text{Am}$  system calculated using the FHF approximation. Each curve corresponds to a specific orientation combination labeled as  $(\theta_P, \theta_T)$ . The solid lines represent the projectile tip orientation ( $\theta_P = 0^\circ$ ), while the dashed lines correspond to the projectile side orientation ( $\theta_P = 90^\circ$ ). Curves of the same color share the same target orientation  $\theta_T$ . The black arrow indicates the incident energy  $E_{c.m.} = 251.9 \text{ MeV}$  selected for the dynamical simulations.

calculated using the frozen Hartree-Fock (FHF) approximation for various orientation combinations [98,100,101]. We observe that the interaction barrier reaches its maximum for the  $(\theta_P, \theta_T) = (90^\circ, 90^\circ)$  configuration, depicted by the green dashed curve. This corresponds to a side-side collision, which represents the most compact geometry, resulting in the strongest Coulomb repulsion. For the dynamical simulations, the incident energy is set to  $E_{c.m.} = 251.9 \text{ MeV}$ , marked by a black arrow in the figure. This energy is selected to lie slightly above the highest interaction barrier to ensure that the system overcomes the Coulomb repulsion for all possible orientation combinations. This guarantees the capture of the projectile and the formation of a composite system across the full angular range.

A key feature revealed by Fig. 1 is the splitting between the potentials for opposite target orientations. This contrast is most pronounced when comparing the  $\theta_T = 0^\circ$  cases, represented by blue curves, with the  $\theta_T = 180^\circ$  cases, shown in purple. Specifically, the potential for the blunt end at  $\theta_T = 0^\circ$  is consistently higher than that for the narrow end at  $\theta_T = 180^\circ$ . This trend holds true for both the projectile tip and side configurations, corresponding to the solid and dashed lines, respectively. Such a difference is a direct manifestation of the non-negligible octupole deformation in  $^{243}\text{Am}$ , which breaks reflection symmetry. Furthermore, this asymmetry diminishes at intermediate angles, as evidenced by the reduced discrepancy between the  $\theta_T = 45^\circ$  (orange) and  $\theta_T = 135^\circ$  (red) curves, regardless of the projectile orientation.

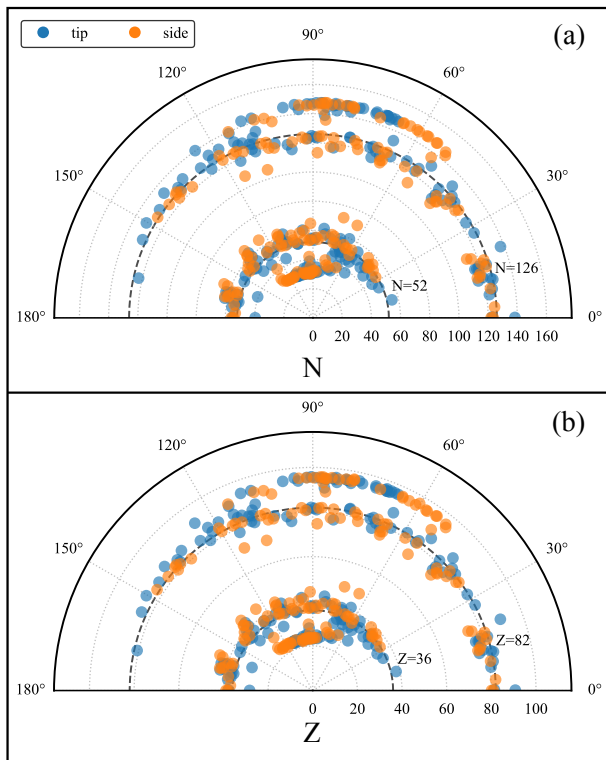


FIG. 2. Polar representation of the final fragment distributions for the  $^{54}\text{Cr} + ^{243}\text{Am}$  reaction. The radial coordinates correspond to (a) neutron number  $N$ , (b) proton number  $Z$ , while the angular coordinate represents the center-of-mass scattering angle. Blue and orange symbols denote the results for the tip and side orientations of the  $^{54}\text{Cr}$  projectile, respectively. The dashed circular arcs indicate the positions of relevant shell gaps  $N = 52, 126$  and  $Z = 36, 82$ .

Following the static analysis in Fig. 1, we investigate the dynamical evolution using the TDHF theory. The calculated fragment scattering angle distributions are displayed in Fig. 2. The radial coordinate corresponds to the neutron number  $N$  and proton number  $Z$  for panels (a) and (b), respectively. The data points in these plots are distinctively partitioned into two regions: the inner region represents the distribution of projectile-like fragments (PLFs), while the outer region corresponds to the target-like fragments (TLFs). Blue points denote the results from the  $^{54}\text{Cr}$  tip orientation, while orange points represent the side orientation. In Fig. 2(a), the outermost and innermost data points, which exhibit nearly constant radial coordinates and form approximate circular arcs confined to a narrow angular range, correspond to quasielastic scattering events. Semicircular arcs at  $N = 52$  and  $N = 126$  are drawn to highlight the locations of the deformed and spherical shell closures, respectively. The target-like QF products are primarily distributed in the vicinity of the spherical  $N = 126$  shell, spanning a broad angular range from  $0^\circ$  to  $150^\circ$ . A closer inspection reveals that most TLF points are located along and slightly inside the  $N = 126$  arc, while the correspond-

ing PLF points are distributed just outside the deformed  $N = 52$  arc. This alignment is consistent with previous studies highlighting the stabilizing role of the octupole deformed shell gaps at  $N = 52\text{--}56$  region during fission and quasifission processes [87,91,102]. In Fig. 2(b), the angular behavior of the proton number  $Z$  mirrors the neutron distribution observed in panel (a). The QF events exhibit a significant drift in proton number away from the entrance channel values  $Z_P = 24$  and  $Z_T = 95$ , with the fragments accumulating along the circular arcs at  $Z = 36$  and  $Z = 82$ , which mark the positions of the deformed and spherical shells, respectively [26,103]. Collectively, these observations indicate that the QF fragments are steered by strong shell effects, associated with both spherical closures and deformed shell gaps.

Complementing the angular view in Fig. 2, the integrated yields allow for a precise quantitative determination of the most probable nucleon numbers. Figure 3 presents these projected distributions for the neutron number  $N$  in panel (a) and proton number  $Z$  in panel (b), obtained by integrating over all contributing impact parameters and the nine sampled  $^{243}\text{Am}$  target orientations. Note that the intense peaks at the extremities, corresponding to quasielastic events, are truncated to enhance the visibility of the QF components, which are the primary focus of this study. We focus first on the projectile side configuration represented by the orange shaded area. In Fig. 3(a), the heavy fragment yield peaks slightly below the  $N = 126$  line. In the complementary region, the light fragment distribution lies predominantly above the  $N = 52$  line, with its peak situated at  $N = 54$ . This pattern may suggest that the deformed shell gaps in the  $N = 52\text{--}56$  region play a crucial role in anchoring the light fragment. In Fig. 3(b), the heavy fragment yield is sharply centered at the spherical  $Z = 82$  shell closure. Simultaneously, the peak for the light fragment is located slightly above the vertical dashed line at  $Z = 36$ .

While these observations might initially suggest a dominant role of the spherical  $Z = 82$  shell in shaping the proton channel, disentangling its specific influence from that of the complementary light fragment presents a fundamental challenge. This ambiguity arises because the total nucleon numbers are rigorously conserved during the binary breakup process. As a result, the formation of a specific heavy fragment automatically dictates the composition of its complementary light partner, and vice versa. Consequently, one cannot definitively distinguish whether the mass equilibration is stopped primarily by the spherical closure of the heavy fragment, the deformed shell gaps of the light fragment, or a cooperative interplay between these coupled shell effects.

In sharp contrast to the strong shell-driven features observed in the side orientation, the tip orientation (blue shades) exhibits fundamentally different dynamics. As shown in Fig. 3, while the side configuration is characterized by sharp, shell-stabilized peaks, the tip yield distribution does not exhibit these prominent features. Instead, the yields are dispersed in the intermediate region

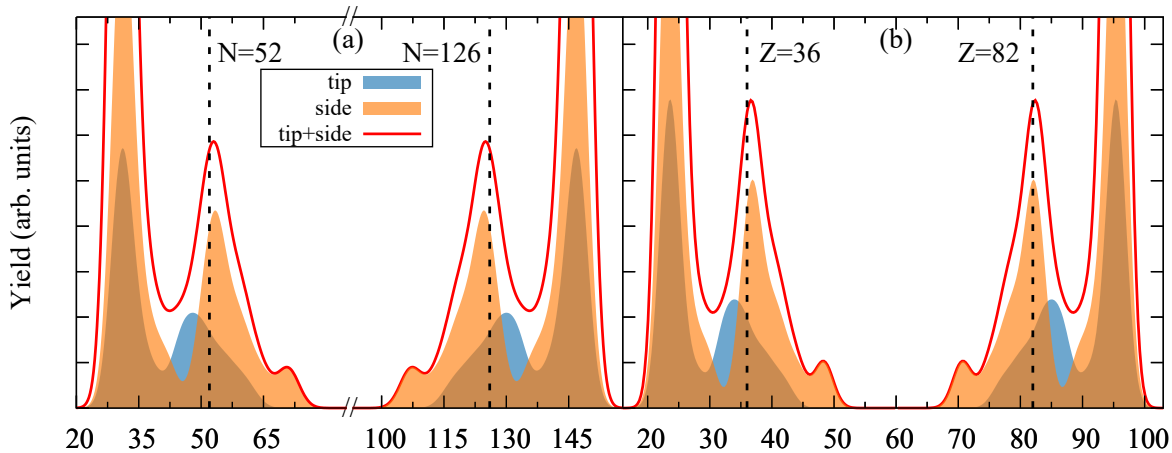


FIG. 3. Fragment yield distributions for the  $^{54}\text{Cr} + ^{243}\text{Am}$  reaction at  $E_{\text{c.m.}} = 251.9$  MeV. The panels display the yields as a function of (a) neutron number  $N$  and (b) proton number  $Z$ . The shaded regions represent the weighted contributions from the  $^{54}\text{Cr}$  tip (blue) and side (orange) orientations, integrated over all contributing impact parameters and nine  $^{243}\text{Am}$  target orientations. The red solid lines denote the total angle-integrated yields. Vertical dashed lines mark the positions of relevant shell gaps at  $N = 52, 126$  and  $Z = 36, 82$ .

bounded by the vertical shell lines and the quasielastic peaks, indicating a lesser degree of net nucleon transfer. This trend is consistent with the observations in Fig. 2, where the tip-orientation data points are broadly distributed between the shell closures and the quasielastic area. The absolute magnitude of these yields is modulated by the geometrical weighting factor  $\sin \theta_P$  inherent in the cross-section calculation, the contribution from the tip collisions is significantly suppressed compared to the side collisions. Consequently, the total yield distribution (red solid line), which represents the sum of the weighted contributions from all orientations, is overwhelmingly determined by the shell-driven dynamics of the side configuration.

The reaction dynamics are further elucidated in Figure 4, which displays the final fragment proton number  $Z$  in panel (a) and neutron number  $N$  in panel (b) as a function of the contact time. The contact time is defined as the time interval during which the minimum density in the neck region exceeds  $0.03 \text{ fm}^{-3}$ . The data reveal that the QF process occurs on a rapid timescale, with the vast majority of QF events concentrated within a contact time window of 5 to 10 zs. Only a small fraction of events exhibit prolonged interaction times, extending up to approximately 20 zs. Comparing the projectile orientations, we observe that the overall duration of the interaction is similar for both the tip and side configurations. However, a notable difference emerges in the nucleon exchange dynamics. Specifically, for a given contact time, the side orientation (orange points) consistently exhibits a larger magnitude of nucleon transfer compared to the tip orientation (blue points). This observation implies that the side configuration, characterized by a more compact contact geometry, facilitates a faster rate of mass equilibration.

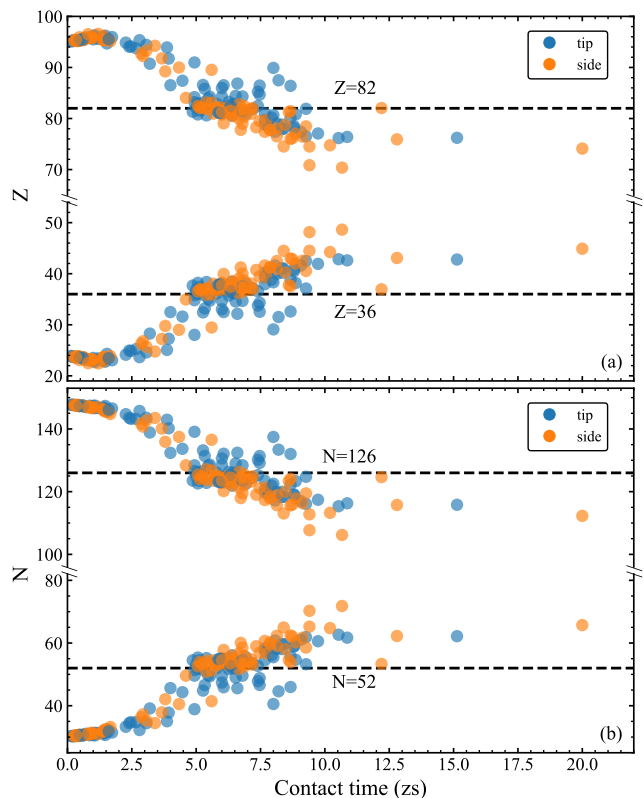


FIG. 4. Fragment (a) proton number  $Z$  and (b) neutron number  $N$  as a function of contact time for the  $^{54}\text{Cr} + ^{243}\text{Am}$  reaction at  $E_{\text{c.m.}} = 251.9$  MeV. The results for the projectile tip (blue points) and side (orange points) orientations are shown separately. Horizontal dashed lines indicate the positions of key spherical and deformed shell gaps.

To extract the mean dynamical trends governing the nucleon transfer, Figure 5 focuses on the statistical properties of the target-like fragments in the dominant region around  $Z \approx 82$ . Given that the TDHF simulations provide continuous expectation values for the final nucleon numbers rather than discrete integers, the data were grouped into bins of width  $\Delta Z = 2$  centered on even numbers. The histogram on the right axis displays the unweighted count of simulation events  $N_{\text{event}}$  for each bin. We observe that this raw count peaks at  $Z = 80$ . It is important to clarify that the difference between this peak and the weighted yield peak at  $Z = 82$  observed in Fig. 3(b) arises simply from the analysis method: the histogram here represents a simple tally of raw trajectories (weight=1), whereas the final yields in Fig. 3 are physically weighted by the impact parameters and orientation probabilities. The black points plotted on the left axis represent the average contact time  $t_{\text{ave}}$  for each  $Z$  bin, where the error bars correspond to the standard deviation. These error bars quantify the dynamical fluctuations in the interaction duration, indicating the spread of contact times for trajectories leading to the same final fragmentation. In the range  $Z = 76$ –80,  $t_{\text{ave}}$  exhibits a linear dependence on the fragment charge, increasing as the system drifts further away from the entrance channel. This behavior is consistent with a classical diffusion scenario, where a larger mass transfer requires a longer interaction time. A dashed line, extending from  $Z = 80$  into the  $Z = 86$  region, is included to guide the eye. Strikingly, as the proton number decreases from  $Z = 86$  towards the shell closure at  $Z = 82$ , the transferred nucleon number increases, but the average contact time remains nearly constant or even decreases, clearly defying the classical diffusion expectation. This anomaly is a distinct signature of the quantum shell effect. As the heavy fragment approaches the magic number  $Z = 82$ , the nuclear structure becomes significantly “stiffer” against deformation. This enhanced rigidity suppresses the elongation of the nuclear neck, leading to a rapid neck rupture and scission process. Consequently, the average contact time in the  $Z = 86$ –82 range forms a plateau, instead of showing the gradual increase that is characteristic of the classical diffusion picture.

Having analyzed the orientation dependence at a fixed energy, we now extend our investigation to the incident energy dependence of the QF dynamics, covering a broad range from below to well above the Coulomb barrier. For this energy-dependent study, we focus specifically on the tip-tip configuration for two main reasons. First, performing a multiple target-projectile orientation analysis across a fine energy grid is computationally prohibitive. Second, our results at  $E_{\text{c.m.}} = 251.9$  MeV indicate that the tip-tip configuration results in significantly less nucleon transfer compared to other orientations. This distinct behavior motivates us to explore the underlying mechanisms governing this specific channel as a function of energy. The simulations cover the range from

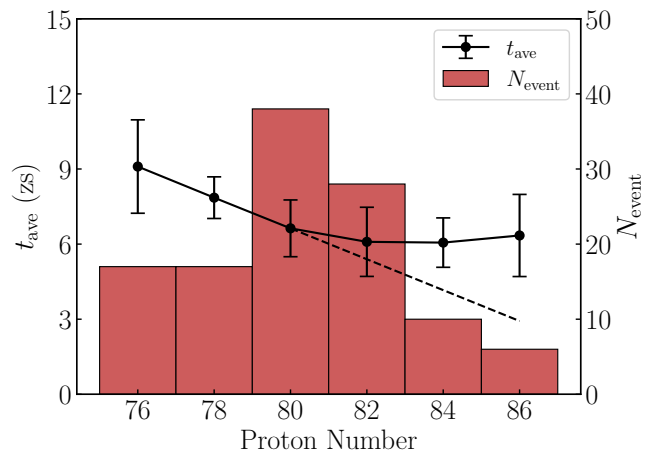


FIG. 5. Statistical analysis of the contact time and event count versus the heavy fragment proton number  $Z$  for the  $^{54}\text{Cr} + ^{243}\text{Am}$  reaction. The solid points refer to the average contact time  $t_{\text{ave}}$  (left axis) calculated for each bin, with error bars corresponding to the standard deviation. The histogram displays the unweighted count of raw TDHF events  $N_{\text{event}}$  (right axis). The data are grouped into bins of width  $\Delta Z = 2$  centered on even proton numbers. The dashed line serves as a guide to the eye.

$E_{\text{c.m.}} = 200$  to 350 MeV with a fine grid step of 2 MeV.

The results presented in Fig. 6 reveal a complex and non-monotonic evolution of the reaction dynamics. Below the Coulomb barrier, the process is dominated by quasielastic scattering. As the energy rises just above the barrier to the range of 218–226 MeV, we observe a sharp increase in nucleon transfer. Interestingly, this trend reverses in the subsequent interval of 226–240 MeV where the magnitude of nucleon transfer decreases. This is followed by a stable plateau between 240 and 280 MeV, with the heavy fragment stabilizing within the blue shaded regions centered at  $Z = 88$  and  $N = 136$ . Notably, these nucleon numbers correspond to  $^{224}\text{Ra}$ , which lies within the well-known region of octupole deformation [104,105]. This suggests that the reaction product is anchored by the stabilizing effects of octupole shell gaps in this energy window. At higher energies from 280 to 300 MeV, the nucleon transfer rises again and eventually enters a regime above 300 MeV where the reaction products exhibit distinct shell features. In this region, the heavy fragments fall within the shaded bands corresponding to the spherical shell closures at  $Z = 82$  and  $N = 126$ . Simultaneously, the complementary light fragments are found within the deformed shell ranges around  $Z = 36$  and  $N = 52$ . These observations suggest that the dynamics in this energy domain are likely shaped by the concurrent influence of spherical closures in the heavy fragment and deformed shell gaps in the light partner.

The clear shift from the octupole-deformed configuration around  $Z \approx 88$  and  $N \approx 136$  observed at intermediate energies to the spherical configuration around  $Z \approx 82$  and  $N \approx 126$  at higher energies explicitly illus-

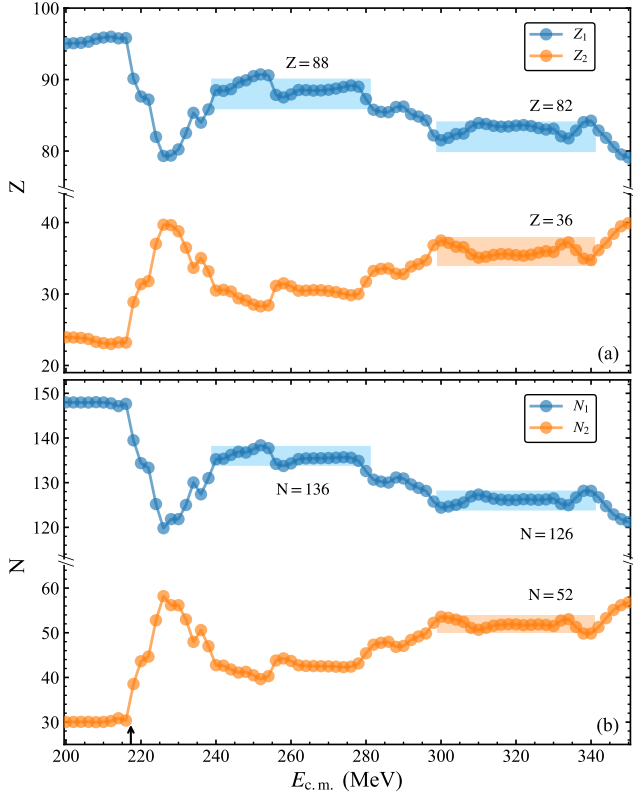


FIG. 6. Fragment (a) proton number  $Z_{1,2}$  and (b) neutron number  $N_{1,2}$  as a function of the incident  $E_{c.m.}$  for the  $^{54}\text{Cr} + ^{243}\text{Am}$  reaction. The results are obtained for central collisions in the fixed tip-tip orientation. The horizontal shaded bands mark the specific shell regions discussed in the text, defined by a width of  $\pm 2$  centered at  $Z = 88$  and  $N = 136$  for the octupole-deformed region,  $Z = 82$  and  $N = 126$  for the spherical shell closure, and  $Z = 36$  and  $N = 52$  for the relevant deformed shells of the light partner. The black arrow indicates the position of the Coulomb barrier at  $V_B = 217.3$  MeV calculated using the FHF approach.

trates the energy dependence of shell effects. This transition parallels the shape evolution with temperature predicted in nuclear structure studies [106], suggesting that the octupole shell effects are more vulnerable to thermal damping and diminish at higher excitation energies, thereby allowing the reaction to be steered by the more resilient spherical shell closure. Collectively, these findings reveal that the reaction is governed not only by the interplay between the spherical and deformed shells of the complementary partners but also by the evolution of the dominant shell structure with incident energy. Understanding this dependence is critical for optimizing the synthesis of SHE, as QF is the primary hindrance to fusion. Our results suggest that by carefully selecting the incident energy, one might avoid energy windows that strongly favor shell-driven QF. For instance, based on our analysis of the tip-tip configuration, the region around  $E_{c.m.} \approx 226$  MeV, where the steering influence of shell effects appears to be suppressed, might represent an op-

timal candidate. While the precise optimal energy may shift when considering integration over all orientations, operating in such a window could potentially diminish the competition from the QF channel, thereby enhancing the relative fusion probability and increasing the likelihood of synthesizing element 119.

#### IV. SUMMARY AND CONCLUSIONS

In this work, we have performed a comprehensive microscopic investigation of QF dynamics in the  $^{54}\text{Cr} + ^{243}\text{Am}$  reaction, a key candidate for synthesizing SHE 119, using the TDHF theory. We systematically explored the influence of projectile-target orientations and the role of incident energy on the reaction outcomes. Our static FHF calculations confirmed that the entrance channel potential is highly sensitive to the initial orientations, particularly due to the octupole deformation of the  $^{243}\text{Am}$  target, which breaks reflection symmetry. The full TDHF dynamical simulations reveal a profound difference in the QF mechanism based on the projectile orientation. For side collisions of  $^{54}\text{Cr}$ , which are found to dominate the total QF yield, the fragment distributions are overwhelmingly governed by shell effects. The heavy fragment production is strongly centered at the  $Z = 82$  spherical shell closure, while the light fragment production is driven by the  $N = 52$ – $56$  deformed shell. In contrast, tip collisions result in relatively smaller nucleon transfer and do not display prominent signatures of shell effects or their competition in the fragment yield distributions. A statistical analysis of the contact times finds that as the heavy fragment proton number approaches the  $Z = 82$  magic shell, the average contact time remains constant or even decreases, contrary to the classical diffusion expectation that more nucleon transfer requires longer time. This behavior is attributed to the quantum shell effect, which provides stability to the fragment's shape, making it less prone to deformation, thereby accelerating neck rupture and reducing the contact time. Furthermore, our investigation of the energy dependence for tip-tip central collisions revealed a complex relationship between the incident energy and shell effects in QF. In different energy regions, the reaction dynamics are governed by specific shell modes (e.g., octupole-deformed vs. spherical shells), their mutual competition, or exhibit suppressed shell influence, clearly demonstrating the energy-dependent nature of these quantum effects. Understanding this energy dependence is crucial for optimizing the conditions for SHE synthesis.

In summary, our microscopic study reveals that the manifestation of shell effects in the final QF fragments is a dynamical outcome sensitively dependent on both the initial orientation and the incident energy. A systematic mapping of this energy dependence is crucial for identifying optimal incident energies, where the system shows suppressed shell influence, thereby enhancing the fusion probability in future experiments. Achieving true

predictive power, however, will require a deeper physical understanding of the origin of this energy dependence and further investigations.

## ACKNOWLEDGMENTS

This work has been supported by the Strategic Priority Research Program of the Chinese Academy of Sci-

ences (Grant No. XDB1550100), and the National Natural Science Foundation of China (Grants No.12435008, No.12375127, and No.12205308).

- 
- [1] A. Sobiczewski and K. Pomorski, *Prog. Part. Nucl. Phys.* **58**, 292 (2007).
- [2] O. R. Smits, C. E. Düllmann, P. Indelicato, W. Nazarewicz, and P. Schwerdtfeger, *Nat. Rev. Phys.* **6**, 86 (2024).
- [3] S. Hofmann and G. Münzenberg, *Rev. Mod. Phys.* **72**, 733 (2000).
- [4] K. Morita, K. Morimoto, D. Kaji, T. Akiyama, S. ichi Goto, H. Haba, E. Ideguchi, R. Kanungo, K. Katori, H. Koura, H. Kudo, T. Ohnishi, A. Ozawa, T. Suda, K. Sueki, H. Xu, T. Yamaguchi, A. Yoneda, A. Yoshida, and Y. Zhao, *J. Phys. Soc. Japan* **73**, 2593 (2004).
- [5] Yu. Ts. Oganessian, V. K. Utyonkov, Yu. V. Lobanov, F. Sh. Abdullin, A. N. Polyakov, R. N. Sagaidak, I. V. Shirokovsky, Yu. S. Tsyganov, A. A. Voinov, G. G. Gulbekian, S. L. Bogomolov, B. N. Gikal, A. N. Mezentsev, S. Iliev, V. G. Subbotin, A. M. Sukhov, K. Subotic, V. I. Zagrebaev, G. K. Vostokin, M. G. Itkis, K. J. Moody, J. B. Patin, D. A. Shaughnessy, M. A. Stoyer, N. J. Stoyer, P. A. Wilk, J. M. Kenneally, J. H. Landrum, J. F. Wild, and R. W. Lougheed, *Phys. Rev. C* **74**, 044602 (2006).
- [6] X. Y. Huang, Z. Y. Zhang, J. G. Wang, L. Ma, C. L. Yang, M. H. Huang, X. L. Wu, Z. G. Gan, H. B. Yang, M. M. Zhang, Y. L. Tian, Y. S. Wang, J. Y. Wang, Y. H. Qiang, G. Xie, S. Y. Xu, Z. Zhao, Z. C. Li, L. C. Sun, L. Zhu, X. Zhang, H. Zhou, F. Guan, Z. H. Li, W. X. Huang, Z. Qin, Y. Wang, X. J. Yin, Y. F. Cui, Z. W. Lu, Y. He, L. T. Sun, Z. Z. Ren, S. G. Zhou, V. K. Utyonkov, A. A. Voinov, Y. S. Tsyganov, A. N. Polyakov, D. I. Solov'yev, N. D. Kovrizhnykh, and M. V. Shumeiko, *Chin. Phys. Lett.* **43**, 010101 (2026).
- [7] Y. T. Oganessian, V. K. Utyonkov, Y. V. Lobanov, F. S. Abdullin, A. N. Polyakov, R. N. Sagaidak, I. V. Shirokovsky, Y. S. Tsyganov, A. A. Voinov, A. N. Mezentsev, V. G. Subbotin, A. M. Sukhov, K. Subotic, V. I. Zagrebaev, S. N. Dmitriev, R. A. Henderson, K. J. Moody, J. M. Kenneally, J. H. Landrum, D. A. Shaughnessy, M. A. Stoyer, N. J. Stoyer, and P. A. Wilk, *Phys. Rev. C* **79**, 024603 (2009).
- [8] S. Hofmann, S. Heinz, R. Mann, J. Maurer, G. Münzenberg, S. Antalic, W. Barth, H. G. Burkhard, L. Dahl, K. Eberhardt, R. Grzywacz, J. H. Hamilton, R. A. Henderson, J. M. Kenneally, B. Kindler, I. Kojouharov, R. Lang, B. Lommel, K. Miernik, D. Miller, K. J. Moody, K. Morita, K. Nishio, A. G. Popeko, J. B. Roberto, J. Runke, K. P. Rykaczewski, S. Saro, C. Scheidenberger, H. J. Schött, D. A. Shaughnessy, M. A. Stoyer, P. Thörle-Pospiech, K. Tinschert, N. Trautmann, J. Uusitalo, and A. V. Yeremin, *Eur. Phys. J. A* **52**, 180 (2016).
- [9] J. Khuyagbaatar, A. Yakushev, C. E. Düllmann, D. Ackermann, L.-L. Andersson, M. Asai, M. Block, R. A. Boll, H. Brand, D. M. Cox, M. Dasgupta, X. Derkx, A. Di Nitto, K. Eberhardt, J. Even, M. Evers, C. Fahlander, U. Forsberg, J. M. Gates, N. Gharibyan, P. Golubev, K. E. Gregorich, J. H. Hamilton, W. Hartmann, R.-D. Herzberg, F. P. Heßberger, D. J. Hinde, J. Hoffmann, R. Hollinger, A. Hübner, E. Jäger, B. Kindler, J. V. Kratz, J. Krier, N. Kurz, M. Laatiaoui, S. Lahiri, R. Lang, B. Lommel, M. Maiti, K. Miernik, S. Minami, A. K. Mistry, C. Mokry, H. Nitsche, J. P. Omtvedt, G. K. Pang, P. Papadakis, D. Renisch, J. B. Roberto, D. Rudolph, J. Runke, K. P. Rykaczewski, L. G. Sarmiento, M. Schädel, B. Schausten, A. Semchenkov, D. A. Shaughnessy, P. Steinegger, J. Steiner, E. E. Tereshatov, P. Thörle-Pospiech, K. Tinschert, T. Torres De Heidenreich, N. Trautmann, A. Türler, J. Uusitalo, M. Wegrzeck, N. Wiehl, S. M. Van Cleve, and V. Yakusheva, *Phys. Rev. C* **102**, 064602 (2020).
- [10] M. Tanaka, P. Brionnet, M. Du, J. Ezold, K. Felker, B. J. Gall, S. Go, R. K. Grzywacz, H. Haba, K. Hagino, S. Hogle, S. Ishizawa, D. Kaji, S. Kimura, T. T. King, Y. Komori, R. K. Lemon, M. G. Leonard, K. Morimoto, K. Morita, D. Nagae, N. Naito, T. Niwase, B. C. Rasco, J. B. Roberto, K. P. Rykaczewski, S. Sakaguchi, H. Sakai, Y. Shigekawa, D. W. Stracener, S. VanCleve, Y. Wang, K. Washiyama, and T. Yokokita, *J. Phys. Soc. Japan* **91**, 084201 (2022).
- [11] J. M. Gates, R. Orford, D. Rudolph, C. Appleton, B. M. Barrios, J. Y. Benitez, M. Bordeau, W. Botha, C. M. Campbell, J. Chadderton, A. T. Chemey, R. M. Clark, H. L. Crawford, J. D. Despotopoulos, O. Dorvaux, N. E. Esker, P. Fallon, C. M. Folden, B. J. P. Gall, F. H. Garcia, P. Golubev, J. A. Gooding, M. Grebo, K. E. Gregorich, M. Guerrero, R. A. Henderson, R.-D. Herzberg, Y. Hrabar, T. T. King, M. Kireeff Covo, A. S. Kirkland, R. Krücken, E. Leistenschneider, E. M. Lykiardopoulou, M. McCarthy, J. A. Mildon, C. Müller-Gatermann, L. Phair, J. L. Pore, E. Rice, K. P. Rykaczewski, B. N. Samsis, L. G. Sarmiento, D. Seweryniak, D. K. Sharp, A. Sinjari, P. Steinegger, M. A. Stoyer, J. M. Szornel, K. Thomas, D. S. Todd, P. Vo, V. Watson, and P. T. Wooddy, *Phys. Rev. Lett.* **133**, 172502 (2024).
- [12] Z. G. Gan, W. X. Huang, Z. Y. Zhang, X. H. Zhou, and H. S. Xu, *Eur. Phys. J. A* **58**, 158 (2022).
- [13] K. Godbey and A. S. Umar, *Front. Phys.* **8**, 40 (2020).
- [14] D. J. Hinde, M. Dasgupta, and E. C. Simpson, *Prog. Part. Nucl. Phys.* **118**, 103856 (2021).
- [15] X.-X. Sun and L. Guo, *Phys. Rev. C* **107**, 064609 (2023).

- [16] B. B. Back, R. R. Betts, K. Cassidy, B. G. Glagola, J. E. Gindler, L. E. Glendenin, and B. D. Wilkins, *Phys. Rev. Lett.* **50**, 818 (1983).
- [17] V. E. Oberacker, A. S. Umar, and C. Simenel, *Phys. Rev. C* **90**, 054605 (2014).
- [18] X.-X. Sun and L. Guo, *Phys. Rev. C* **105**, 054610 (2022).
- [19] D. J. Hinde, M. Dasgupta, J. R. Leigh, J. P. Lestone, J. C. Mein, C. R. Morton, J. O. Newton, and H. Timmers, *Phys. Rev. Lett.* **74**, 1295 (1995).
- [20] K. Nishio, S. Mitsuoka, I. Nishinaka, H. Makii, Y. Wakabayashi, H. Ikezoe, K. Hirose, T. Ohtsuki, Y. Aritomo, and S. Hofmann, *Phys. Rev. C* **86**, 034608 (2012).
- [21] A. Wakhle, C. Simenel, D. J. Hinde, M. Dasgupta, M. Evers, D. H. Luong, R. du Rietz, and E. Williams, *Phys. Rev. Lett.* **113**, 182502 (2014).
- [22] A. S. Umar, C. Simenel, and W. Ye, *Phys. Rev. C* **96**, 024625 (2017).
- [23] L. Guo, C. Shen, C. Yu, and Z. Wu, *Phys. Rev. C* **98**, 064609 (2018).
- [24] C. Simenel, K. Godbey, and A. S. Umar, *Phys. Rev. Lett.* **124**, 212504 (2020).
- [25] A. Sen, T. K. Ghosh, E. M. Kozulin, I. M. Itkis, G. N. Knyazheva, K. V. Novikov, S. Bhattacharya, K. Banerjee, and C. Bhattacharya, *Phys. Rev. C* **105**, 014627 (2022).
- [26] M. Morjean, D. J. Hinde, C. Simenel, D. Y. Jeung, M. Airiau, K. J. Cook, M. Dasgupta, A. Drouart, D. Jacquet, S. Kalkal, C. S. Palshetkar, E. Prasad, D. Rafferty, E. C. Simpson, L. Tassan-Got, K. VoPhuoc, and E. Williams, *Phys. Rev. Lett.* **119**, 222502 (2017).
- [27] G. Mohanto, D. J. Hinde, K. Banerjee, M. Dasgupta, D. Y. Jeung, C. Simenel, E. C. Simpson, A. Wakhle, E. Williams, I. P. Carter, K. J. Cook, D. H. Luong, C. S. Palshetkar, and D. C. Rafferty, *Phys. Rev. C* **97**, 054603 (2018).
- [28] L. Li, L. Guo, K. Godbey, and A. S. Umar, *Phys. Lett. B* **833**, 137349 (2022).
- [29] G. G. Adamian, N. V. Antonenko, and W. Scheid, *Phys. Rev. C* **68**, 034601 (2003).
- [30] N. Wang, E.-G. Zhao, W. Scheid, and S.-G. Zhou, *Phys. Rev. C* **85**, 041601(R) (2012).
- [31] L. Zhu, J. Su, C. Li, and F.-S. Zhang, *Phys. Lett. B* **829**, 137113 (2022).
- [32] X.-Q. Deng and S.-G. Zhou, *Phys. Rev. C* **107**, 014616 (2023).
- [33] Z.-H. Wang, P.-H. Chen, Y.-L. Zhang, M.-H. Huang, and Z.-Q. Feng, *Phys. Rev. C* **113**, 014607 (2026).
- [34] V. Zagrebaev and W. Greiner, *J. Phys. G: Nucl. Part. Phys.* **34**, 2265 (2007).
- [35] S. Chopra, M. K. Sharma, P. O. Hess, Hemdeep, and NeetuMaan, *Phys Rev C* **103**, 064615 (2021).
- [36] N. Wang and L. Guo, *Phys. Lett. B* **760**, 236 (2016).
- [37] X. Chen, J. Yang, Y. Cui, K. Zhao, Z. Li, and Y. Zhang, *Phys. Rev. C* **109**, L021604 (2024).
- [38] P. Feng, K. Zhao, Z. Liu, N. Wang, F.-S. Zhang, and Y. Zhang, *Phys. Rev. C* **111**, 024603 (2025).
- [39] Y. Feng, Y. Huang, E. Xiao, X. Lei, L. Zhu, and J. Su, *Phys. Rev. C* **107**, 044606 (2023).
- [40] S. Ayik, M. Arik, E. C. Karanfil, O. Yilmaz, B. Yilmaz, and A. S. Umar, *Phys. Rev. C* **104**, 054614 (2021).
- [41] K. Sekizawa, S. Ayik, E. C. Karanfil, M. Arik, O. Yilmaz, and A. S. Umar, *Phys. Rev. C* **112**, 024612 (2025).
- [42] R. Balian and M. Vénéroni, *Phys. Lett. B* **136**, 301 (1984).
- [43] E. Williams, K. Sekizawa, D. J. Hinde, C. Simenel, M. Dasgupta, I. P. Carter, K. J. Cook, D. Y. Jeung, S. D. McNeil, C. S. Palshetkar, D. C. Rafferty, K. Ramachandran, and A. Wakhle, *Phys. Rev. Lett.* **120**, 022501 (2018).
- [44] D. D. Zhang, B. Li, D. Vretenar, T. Nikšić, Z. X. Ren, P. W. Zhao, and J. Meng, *Phys. Rev. C* **109**, 024316 (2024).
- [45] T. Nakatsukasa, K. Matsuyanagi, M. Matsuo, and K. Yabana, *Rev. Mod. Phys.* **88**, 045004 (2016).
- [46] C. Simenel and A. S. Umar, *Prog. Part. Nucl. Phys.* **103**, 19 (2018).
- [47] P. D. Stevenson and M. C. Barton, *Prog. Part. Nucl. Phys.* **104**, 142 (2019).
- [48] K. Sekizawa, *Front. Phys.* **7**, 20 (2019).
- [49] X.-X. Sun and L. Guo, *Commun. Theor. Phys.* **74**, 097302 (2022).
- [50] C. Simenel, *Eur. Phys. J. A* **61**, 181 (2025).
- [51] J. W. Negele, *Rev. Mod. Phys.* **54**, 913 (1982).
- [52] L. Guo, J. A. Maruhn, and P.-G. Reinhard, *Phys. Rev. C* **76**, 014601 (2007).
- [53] C. Simenel, P. Chomaz, and G. de France, *Phys. Rev. C* **76**, 024609 (2007).
- [54] L. Guo, J. A. Maruhn, P.-G. Reinhard, and Y. Hashimoto, *Phys. Rev. C* **77**, 041301(R) (2008).
- [55] Cédric Simenel and Benoit Avez, *Intl. J. Mod. Phys. E* **17**, 31 (2008).
- [56] A. S. Umar, V. E. Oberacker, and C. Simenel, *Phys. Rev. C* **92**, 024621 (2015).
- [57] K. Sekizawa and K. Yabana, *Phys. Rev. C* **93**, 054616 (2016).
- [58] P. D. Stevenson, *Front. Phys.* **10**, 1019285 (2022).
- [59] C. Simenel, A. S. Umar, K. Godbey, and P. McGlynn, *Phys. Lett. B* **871**, 139955 (2025).
- [60] Z. Wu, X.-X. Sun, and L. Guo, *Phys. Rev. C* **113**, 024618 (2026).
- [61] K. Sekizawa and K. Yabana, *Phys. Rev. C* **88**, 014614 (2013).
- [62] Z. Wu and L. Guo, *Phys. Rev. C* **100**, 014612 (2019).
- [63] X. Li, Z. Wu, and L. Guo, *Sci. China-Phys. Mech. Astron.* **62**, 122011 (2019).
- [64] X. Jiang and N. Wang, *Phys. Rev. C* **101**, 014604 (2020).
- [65] C. Simenel, K. Godbey, H. Lee, P. McGlynn, and A. S. Umar, *Nucl. Phys. A* **1062**, 123170 (2025).
- [66] C. Simenel, *Phys. Rev. Lett.* **105**, 192701 (2010).
- [67] G.-F. Dai, L. Guo, E.-G. Zhao, and S.-G. Zhou, *Phys. Rev. C* **90**, 044609 (2014).
- [68] K. Sekizawa and K. Hagino, *Phys. Rev. C* **99**, 051602(R) (2019).
- [69] P. D. Stevenson, E. B. Suckling, S. Fracasso, M. C. Barton, and A. S. Umar, *Phys. Rev. C* **93**, 054617 (2016).
- [70] K. Godbey, L. Guo, and A. S. Umar, *Phys. Rev. C* **100**, 054612 (2019).
- [71] X.-X. Sun, L. Guo, and A. S. Umar, *Phys. Rev. C* **105**, 034601 (2022).
- [72] X.-X. Sun and L. Guo, *Phys. Rev. C* **107**, L011601 (2023).
- [73] H. Yao, H. Yang, and N. Wang, *Phys. Rev. C* **110**, 014602 (2024).
- [74] X. Jiang, R. An, and N. Wang, *Phys. Rev. C* **112**, L051603 (2025).
- [75] C. Simenel and A. S. Umar, *Phys. Rev. C* **89**, 031601(R) (2014).

- (2014).
- [76] P. M. Goddard, P. D. Stevenson, and A. Rios, *Phys. Rev. C* **92**, 054610 (2015).
- [77] Y. Huang, X.-X. Sun, and L. Guo, *Eur. Phys. J. A* **60**, 100 (2024).
- [78] Y. Huang, X.-X. Sun, and L. Guo, *Phys. Rev. C* **110**, 064318 (2024).
- [79] Y. Qiang, J. Pei, and K. Godbey, *Phys. Lett. B* **861**, 139248 (2025).
- [80] K. Sekizawa, *Phys. Rev. C* **96**, 041601(R) (2017).
- [81] Z. Wu and L. Guo, *Sci. China-Phys. Mech. Astron.* **63**, 242021 (2020).
- [82] Z. Wu, L. Guo, Z. Liu, and G. Peng, *Phys. Lett. B* **825**, 136886 (2022).
- [83] C. Simenel, P. Chomaz, and G. de France, *Phys. Rev. Lett.* **86**, 2971 (2001).
- [84] P.-G. Reinhard, Lu Guo, and J. A. Maruhn, *Eur. Phys. J. A* **32**, 19 (2007).
- [85] C. Simenel and P. Chomaz, *Phys. Rev. C* **80**, 064309 (2009).
- [86] A. S. Umar, V. E. Oberacker, and C. Simenel, *Phys. Rev. C* **94**, 024605 (2016).
- [87] C. Simenel, P. McGlynn, A. S. Umar, and K. Godbey, *Phys. Lett. B* **822**, 136648 (2021).
- [88] K. Hammerton, Z. Kohley, D. J. Hinde, M. Dasgupta, A. Wakhle, E. Williams, V. E. Oberacker, A. S. Umar, I. P. Carter, K. J. Cook, J. Greene, D. Y. Jeung, D. H. Luong, S. D. McNeil, C. S. Palshetkar, D. C. Rafferty, C. Simenel, and K. Stiefel, *Phys. Rev. C* **91**, 041602(R) (2015).
- [89] A. S. Umar and V. E. Oberacker, *Nucl. Phys. A* **944**, 238 (2015).
- [90] C. Yu and L. Guo, *Sci. China-Phys. Mech. Astron.* **60**, 092011 (2017).
- [91] K. Godbey, A. S. Umar, and C. Simenel, *Phys. Rev. C* **100**, 024610 (2019).
- [92] L. Li, L. Guo, K. Godbey, and A. S. Umar, *Phys. Rev. C* **110**, 064607 (2024).
- [93] C. Simenel, R. Bernard, G. Blanchon, K. Godbey, H. Lee, P. McGlynn, and A. S. Umar, *EPJ Web Conf.* **306**, 01019 (2024).
- [94] E. Chabanat, P. Bonche, P. Haensel, J. Meyer, and R. Schaeffer, *Nucl. Phys. A* **635**, 231 (1998).
- [95] Abhishek, P. Stevenson, Y. Shi, E. Yüksel, and A. S. Umar, *Comp. Phys. Comm.* **301**, 109239 (2024).
- [96] G. Dai, L. Guo, E. Zhao, and S. Zhou, *Sci. China-Phys. Mech. Astron.* **57**, 1618 (2014).
- [97] L. Shi and L. Guo, *Nucl. Phys. Rev.* **34**, 41 (2017).
- [98] L. Guo, C. Simenel, L. Shi, and C. Yu, *Phys. Lett. B* **782**, 401 (2018).
- [99] L. Guo, K. Godbey, and A. S. Umar, *Phys. Rev. C* **98**, 064607 (2018).
- [100] K. Washiyama and D. Lacroix, *Phys. Rev. C* **78**, 024610 (2008).
- [101] L. Guo and T. Nakatsukasa, *EPJ Web Conf.* **38**, 09003 (2012).
- [102] G. Scamps and C. Simenel, *Phys. Rev. C* **100**, 041602(R) (2019).
- [103] E. M. Kozulin, G. N. Knyazheva, I. M. Itkis, M. G. Itkis, Y. S. Mukhamejanov, A. A. Bogachev, K. V. Novikov, V. V. Kirakosyan, D. Kumar, T. Banerjee, M. Cheralu, M. Maiti, R. Prajapat, R. Kumar, G. Sarkar, W. H. Trzaska, A. N. Andreyev, I. M. Harca, A. Mitu, and E. Vardaci, *Phys. Rev. C* **105**, 014607 (2022).
- [104] P. A. Butler, L. P. Gaffney, P. Spagnoletti, K. Abrahams, M. Bowry, J. Cederkäll, G. de Angelis, H. De Witte, P. E. Garrett, A. Goldkuhle, C. Henrich, A. Illana, K. Johnston, D. T. Joss, J. M. Keatings, N. A. Kelly, M. Komorowska, J. Konki, T. Kröll, M. Lozano, B. S. Nara Singh, D. O'Donnell, J. Ojala, R. D. Page, L. G. Pedersen, C. Raison, P. Reiter, J. A. Rodriguez, D. Rosiak, S. Rothe, M. Scheck, M. Seidlitz, T. M. Shneidman, B. Siebeck, J. Sinclair, J. F. Smith, M. Stryczyk, P. Van Duppen, S. Vinals, V. Virtanen, N. Warr, K. Wrzosek-Lipska, and M. Zielińska, *Phys. Rev. Lett.* **124**, 042503 (2020).
- [105] H. Wollersheim, H. Emling, H. Grein, R. Kulesa, R. Simon, C. Fleischmann, J. de Boer, E. Hauber, C. Lauterbach, C. Schandera, P. Butler, and T. Czosnyka, *Nucl. Phys. A* **556**, 261 (1993).
- [106] W. Zhang and Y. F. Niu, *Phys. Rev. C* **96**, 054308 (2017).